APPLIED SCIENCES AND ENGINEERING

Adhesive nonfibrotic bioelectronic interfaces on diverse peripheral nerves for long-term functional neuromodulation

Hyunmin Moon[1], Bastien F. G. Aymon[1], Jue Deng[1], Tao Zhou[2], Vincent Prevosto[3], Fan Wang[3], Jingjing Wu[1]*, Xuanhe Zhao[1,4]*

Bioelectronic devices implanted on peripheral nerves offer potential for the treatment and rehabilitation of clinical diseases. However, the foreign body reaction and the subsequent fibrous capsule formation at the device–peripheral nerve interface severely limit their efficacy and longevity in vivo. Here, we describe a robust bioadhesive strategy that can establish nonfibrotic bioelectronic interfaces on diverse peripheral nerves—occipital, vagus, deep peroneal, sciatic, tibial, and common peroneal nerves—for up to 12 weeks. Our approach inhibits the infiltration of immune cells into the interface, thereby preventing the formation of fibrous capsules in the inflammatory microenvironment. We demonstrate that our adhesive bioelectronic device with nonfibrotic interfaces maintains long-term blood pressure regulation in a spontaneously hypertensive rat model over 4 weeks. Furthermore, we confirm minimal accumulation of macrophages, smooth muscle actin, and collagen at nonfibrotic bioelectronic interfaces after 12 weeks of device implantation with nerve stimulation, supporting long-lasting neuromodulation without fibrosis.

INTRODUCTION

Bioelectronic devices applied to the peripheral nervous system represent a promising avenue in translational medicine (*1*–*3*). Peripheral nerve pathways, comprising the autonomic, somatic, and enteric nervous systems, are intimately connected to the central nervous system and extend throughout the body (*4*, *5*). Bioelectronic modulation of diverse peripheral nerves has demonstrated its clinical efficacy in treating a spectrum of conditions, including chronic migraine (*6*, *7*), stroke (*8*, *9*), epilepsy (*10*, *11*), depression (*12*), gait disorder (*13*, *14*), overactive bladder (*15*, *16*), and hypertension (*17*) (Fig. 1A). These clinical treatments through peripheral nerve stimulation often serve as the only alternative to chemical-based therapies for drug-resistant patients, and the technology continues to evolve (*1*, *3*).

A key challenge for the long-term reliability and integration of bioelectronic interfaces with peripheral nerves lies in the foreign body reaction (FBR). FBR remains the primary cause of bioelectronic device failure in vivo (*18*–*20*). Innate immune cells initially infiltrate the interface, triggering an inflammatory response that leads to the formation of a densely cellularized FBR, including macrophages and multinucleated giant cells (*21*, *22*). Over time, fibroblast activation results in a collagen-rich fibrous capsule deposition at the interface between the implanted bioelectronic device and the peripheral nerve (Fig. 1B). Chronic FBR results in thickening of these fibrous capsules, thereby considerably deteriorating the electrical performance at the interface during recording and stimulation and ultimately compromising the longevity of bioelectronic devices (*22*–*25*). To address the challenges introduced by FBR, several material design strategies have emerged, including ultrasoft (*26*–*28*), hydrophilic (*29*–*31*), lubricious (*32*, *33*), drug-eluting (*34*), zwitterionic (*35*–*37*), biomolecule-conjugated (*38*, *39*), and mechanically actuating (*40*–*42*) properties. Despite these efforts to mitigate fibrosis, none of these previous attempts successfully managed to fully prevent it, as the occurrence of FBR is largely material agnostic (*42*, *43*).

Here, we propose that robust adhesion at the interface between the bioelectronic device and the peripheral nerve can fully prevent the formation of fibrous capsules. A bioadhesive hydrogel enables conformal contact of the bioelectronic interfaces via covalent bonds with the surface of peripheral nerves. This adhesion inhibits immune cell infiltration into the interface and the subsequent fibrous capsule formation (Fig. 1C). Consequently, adhesion facilitates electrical stimulation or recording of peripheral nerves while also preventing mechanically driven FBR (*43*, *44*) induced by micromotion at the interface. In this study, we developed an adhesive nonfibrotic bioelectronics (ANB) to achieve reliable long-term implantation on diverse nerves without fibrous capsule formation at the interface. The ANB can envelop and adhere to peripheral nerves of different sizes at various sites in vivo. For example, the ANB can be applied to the small-sized deep peroneal nerve (DPN), and its interface with the thick sciatic nerve exhibited robust and intimate contact (Fig. 1D). In addition, the nonfibrotic property of the ANB interface on various peripheral nerves was validated through histological and immunofluorescence studies over 12 weeks. Upon mechanical and electrical evaluations, the ANB achieved highly soft, flexible, stretchable, adhesive, and conductive material properties, essential for long-term stable communication with peripheral nerves in physiological environments. Furthermore, the ANB effectively regulated blood pressure (BP) in a spontaneously hypertensive rat model through long-term stable stimulation of DPN over 4 weeks, demonstrating its potential for clinical translation.

RESULTS

Design and implementation of the ANB

The ANB was designed for an adhesion-based implantation on various peripheral nerves using biocompatible materials, including a

[1]Department of Mechanical Engineering, Massachusetts Institute of Technology, Cambridge, MA 02139, USA. [2]Department of Engineering Science and Mechanics, Pennsylvania State University, University Park, PA 16802, USA. [3]McGovern Institute for Brain Research, Department of Brain and Cognitive Sciences, Massachusetts Institute of Technology, Cambridge, MA 02139, USA. [4]Department of Civil and Environmental Engineering, Massachusetts Institute of Technology, Cambridge, MA 02139, USA.
*Corresponding author. Email: wujj@mit.edu (J.W.); zhaox@mit.edu (X.Z.)

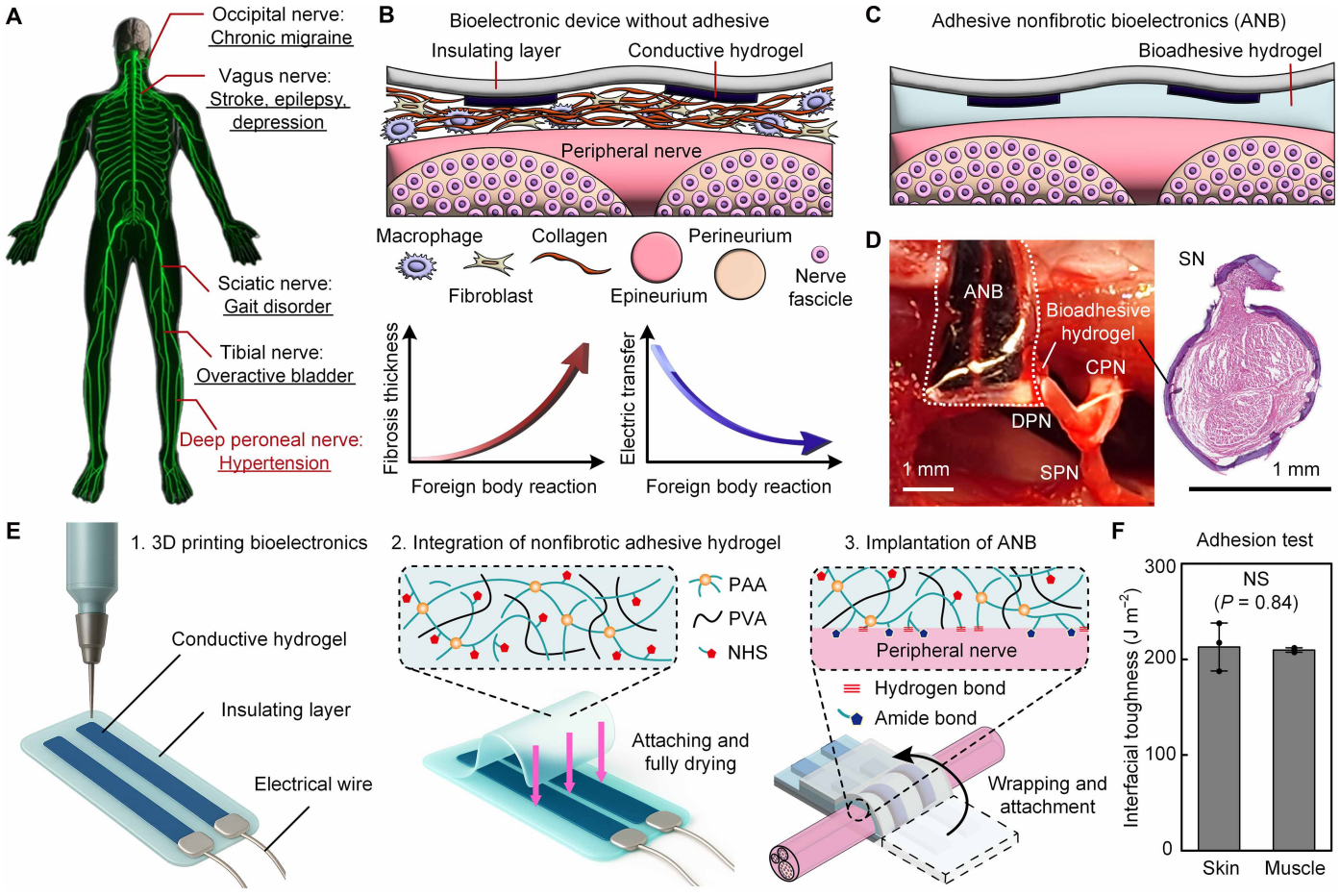

Fig. 1. Design and mechanism of the adhesive nonfibrotic bioelectronics as a strategy for nonfibrotic interfaces. (**A**) Schematic illustration of the clinical applications of bioelectronic devices in treating diseases. (**B**) Schematic depicting the limitations imposed by fibrous capsule formation on nerves. Active foreign body reaction (FBR) results in thick fibrosis and impedes electric transfer, leading to the failure of bioelectronic devices. (**C**) Mechanism of the adhesive nonfibrotic bioelectronics (ANB) to establish nonfibrotic interfaces using the bioadhesive hydrogel, enabling intact electrical stimulation. (**D**) Images of the ANB with nonfibrotic interfaces. The ANB was implanted in a robust and intimate manner in the deep peroneal nerve (DPN) separated from a superficial peroneal nerve (SPN) in a common peroneal nerve (CPN). The bioadhesive hydrogel of the ANB formed conformal contact with the sciatic nerve (SN) and prevented fibrous capsule formation. (**E**) Schematic illustrations for the fabrication and implantation of the ANB: (1) Patterning the insulating layer and the conductive hydrogel by three-dimensional (3D) printing. (2) Integrating the nonfibrotic adhesive hydrogel on the bioelectronic device and fully drying. (3) Wrapping the ANB around DPN and pressing for 5 s at the interface to generate amide and hydrogen bonds. (**F**) Resultant interfacial toughness of the ANB in contact with biological tissue. Each experiment was repeated independently ($n = 3$). Statistical significance and P values are determined by two-sided unpaired t test [NS (not significant)].

polyurethane(PU)insulatinglayer,apoly(3,4-ethylenedioxythiophene) polystyrene sulfonate (PEDOT:PSS) conductive hydrogel, and a poly(vinyl alcohol)/poly(acrylic acid) (PVA/PAA)–based bioadhesive hydrogel (Fig. 1E) (*45*, *46*). Because of the small size of rat peripheral nerves (300 to 1200 μm in diameter), a multimaterial three-dimensional (3D) printing technique was used to precisely pattern the insulating layer and conductive hydrogel, which enabled fast, convenient, and precise fabrication of the bioelectronic device with a resolution of 100 μm (fig. S1) in 10 minutes (fig. S2).

A bioadhesive hydrogel film was prepared separately following a previously established protocol (fig. S3) (*46*, *47*). The bioadhesive hydrogel film was prestretched to match its swelling ratio and attached to the 3D printed bioelectronic device right after cross-linking, after which the assembly was dried. Upon contact with peripheral nerves, the dry bioadhesive layer absorbed interfacial moisture to allow the formation of hydrogen (physical cross-linking) and amide bonds (covalent cross-linking) (fig. S4). Although rehydration may transiently alter local pH or ionic balance, these effects quickly equilibrate and did not produce detectable irritation or fibrosis in our in vivo studies. This adhesion mechanism, based on *N*-hydroxysuccinimide (NHS)–amine covalent coupling, was directly validated in our prior studies using amine-functionalized fluorescent probes (*46*) and was further confirmed with a fluorescently coupled primary amine (fig. S5). The resultant adhesion with ex vivo tissue exhibited high interfacial toughness of more than 200 J m^{-2} (Fig. 1F, fig. S6, and movie S1). Beyond tough adhesion, the ANB also maintained stability without substantial device swelling after an accelerated aging period of 12 weeks under physiological conditions (95% relative humidity; fig. S7). Last, its biocompatibility was confirmed through cytotoxicity assays (fig. S8), which showed no detectable decrease in the in vitro viability of mouse embryonic fibroblasts exposed to ANB-conditioned medium for 24 hours.

The ANB showed favorable mechanical properties for long-term implantation, including a low Young's modulus (~0.75 MPa), large maximum stretch (>1000%), and high tensile strength (~6.8 MPa) (figs. S9 and S10 and movie S2). Moreover, the bioadhesive hydrogel layer in direct contact with peripheral nerves exhibited a Young's modulus (~0.1 MPa) comparable to that of the rat nerve epineurium (~0.4 ± 0.1 MPa) (*48*), ensuring mechanical compatibility with the host tissue. To further assess the durability of the assembled structure under repeated strain, we subjected the device to 10,000 tensile cycles at 20% strain (fig. S10). The device remained intact with no evidence of delamination among layers. Overall, the high compliance and stretchability of the ANB accommodated the natural motion of peripheral nerves in response to body movement, thereby improving its long-term stability in vivo.

Nonfibrotic interfaces

To verify that our adhesive bioelectronic interface remains nonfibrotic 4 weeks after implantation of the ANB, we examined fibrous capsules on the surface of peripheral nerves in a Sprague Dawley (SD) rat model through histological analysis using hematoxylin and eosin (H&E) and Masson's trichrome (MT) staining. We compared three groups: (i) native tissue, where no implant is present; (ii) adhesive interfaces, where the ANB was attached for 4 weeks; and (iii) nonadhesive interfaces, where the ANB was first fully swollen in sterile phosphate-buffered saline (PBS) to remove the hydrogel's adhesive properties and then sutured on the nerves (Fig. 2). To demonstrate the versatility of the ANB, we considered peripheral nerves of different sizes (300 to 1200 μm in diameter) located throughout the rat's body, from its head to its leg, including the occipital, vagus, deep peroneal, sciatic, tibial, and common peroneal nerves (Fig. 2A and fig. S12). Native tissue showed an intact surface around the epineurium (Fig. 2B). Likewise, adhesive interfaces showed no visible fibrous capsule formation and were comparable to the native tissue group for all nerves considered. Histological analysis by blinded pathologists indicated that the ANB with adhesive interfaces prevented fibrous capsule formation and inflammation of the peripheral nerves. There was also no apoptosis of axons during long-term implantation (Fig. 2C). On the other hand, all nonadhesive interfaces exhibited thick and densely cellularized fibrous capsules at the outer epineurium of nerves, including fat tissue necrosis and subsequent scar tissue formation (Fig. 2D). We magnified the interfaces between the ANB and the sciatic nerve (Fig. 2, E to G). For native tissue and adhesive interfaces, the epineurium layer was defined because fibrous capsules were not formed. On the contrary, the thick fibrous capsule around the nonadhesive interfaces obscured the boundary of the outer epineurium. Similar results were observed in all other nerves (fig. S13).

To quantify the differences between the three groups, we further measured the thickness of the outer epineurium, including fibrous capsules when present (Fig. 2H). The thicknesses of the outer epineurium were similar in native tissue and adhesive interfaces for all nerve samples. This result confirmed that the interface remained nonfibrotic following the implantation of the ANB, suggesting that adhesion is a robust strategy to prevent chronic inflammation around nerves. Conversely, nonadhesive interfaces showed a thick outer epineurium due to fibrous capsule formation on nerves (Fig. 2H).

Electrical properties and stability

To evaluate the potential of the ANB for long-term implantation and stable stimulation, we measured its electrical properties, which exhibited favorable performance with regards to its impedance ($\lfloor Z \rfloor$ ~ 0.76 kilohm at 1 kHz; see Fig. 3A), conductivity (σ ~ 2.3 S cm^{-1}; see Fig. 3B), charge storage capacity (CSC ~ 10.5 mC cm^{-2}; see Fig. 3, C and E), and charge injection capacity (CIC ~ 290 μC cm^{-2}; see Fig. 3, D and E). These electrical properties of the ANB were compared with those of a Pt electrode, a pure adhesive, and the 3D printed bioelectronic device only (i.e., without the bioadhesive hydrogel). We determined the corrosion-resistant window from each material, ranging from maximum anodic potential (E_{ma}) to maximum cathodic potential (E_{mc}) as the input boundary for CSC and CIC measurements (fig. S14). The pure adhesive had impedance ($\lfloor Z \rfloor$ ~ 1.17 kilohm at 1 kHz), conductivity (σ ~ 0.4 S cm^{-1}), CSC (~0.5 mC cm^{-2}), and CIC (~93 μC cm^{-2}). Although applying the bioadhesive hydrogel slightly reduced overall performance, the ANB still exhibited high-quality electrical properties for stimulation, including high CSC and CIC. This was achieved because the hydrogel provided sufficient conductivity to enable charge transfer from the electrodes to the nerves, while the relatively large separation between cathodic and anodic electrodes prevented cross-talk. As a result, charges injected from the electrodes could not travel directly through the hydrogel between sites (fig. S15).

Furthermore, we analyzed CSC and CIC changes under cyclic electrical and mechanical testing, and soaking in PBS at room temperature (RT), to confirm the long-term stability of the ANB. The electrical performance improved with a 43% increase in CSC over 100,000 charging and discharging cycles (Fig. 3F). Although an 18% decrease in CIC occurred over 100,000 CIC cycles, it remained sufficiently high to stimulate the nerve in vivo. Moreover, CSC and CIC of the ANB were maintained or improved over 10,000 tensile cycles (100% stretch) and 12 weeks of soaking in PBS at RT (Fig. 3, G and H).

Long-term in vivo BP regulation

To evaluate the efficacy and importance of nonfibrotic interfaces in bioelectronic devices, we stimulated DPN for 4 weeks using the ANB or the nonadhesive device (Fig. 4). We monitored the BP and heart rate (HR) of spontaneously hypertensive rats via a noninvasive tail cuff upon DPN stimulation once per week (Fig. 4A). We chose BP regulation as the primary functional readout because it represents a sensitive, whole-organism measure of DPN conduction. Even minor conduction deficits would be expected to blunt this systemic response, making BP a more translationally relevant indicator than local electroneurographic recording. To compare BP and HR between spontaneously hypertensive rats and normal rats, we first recorded them without stimulation (Fig. 4B). The BP of the spontaneously hypertensive rats ranged from 113 to 120 mmHg, whereas that of the normal rats showed a lower level of 76 to 85 mmHg. A similar resting HR of ~400 beats per minute (bpm) was observed in both groups.

To regulate BP in spontaneously hypertensive rats using DPN stimulation, we then applied different current pulses by varying their amplitude (0.1 to 1.0 mA), width (100 to 1000 μs), and number ($N = 1$ to 200 pulses) (Fig. 4, C to E). To identify lower bounds on the stimulation parameters, we first found that leg extension commenced at a stimulation pulse of 0.2 mA and 100 μs, indicating a charge threshold of 20 nC. These base pulse parameters (0.2 mA, 100 μs, and $N = 1$) were then systematically increased, and their effect was analyzed.

We observed a gradual BP decrease upon stimulation with an increasing value of each pulse parameter, accompanied by more

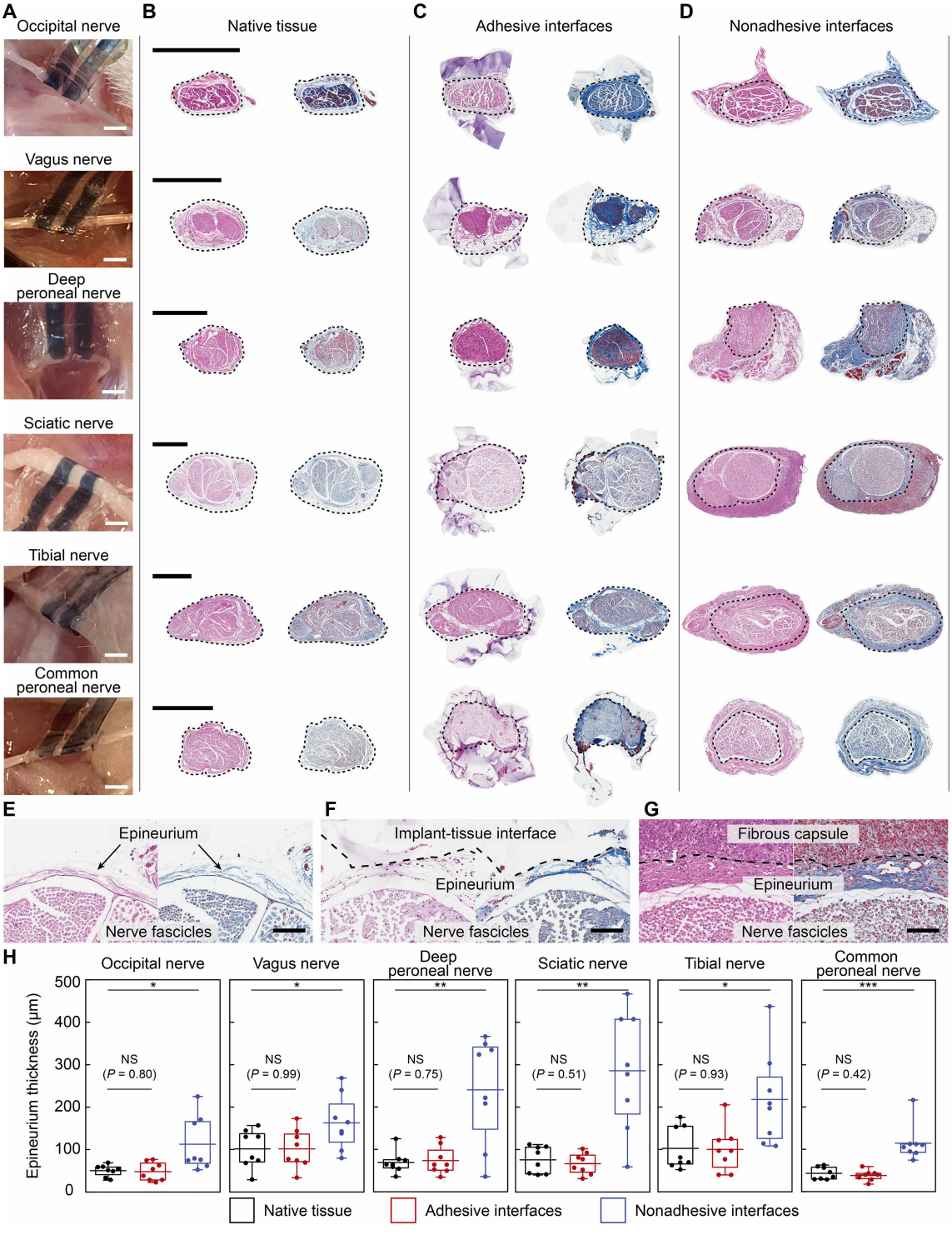

Fig. 2. Validation of nonfibrotic bioelectronic interfaces. (**A**) ANB implantation on diverse peripheral nerves for 4 weeks. Occipital, vagus, deep peroneal, sciatic, tibial, and CPNs were used. Scale bars, 1 mm. (**B** to **D**) Representative histological images of the peripheral nerves before and after 4 weeks of implantation of the bioelectronic devices, comparing three groups: native tissue (B), adhesive interfaces (C), and nonadhesive interfaces (D). Each nerve was stained with H&E (left) and MT (right). Dashed lines indicate the outer epineurium of the nerve. Scale bars, 500 μm. (**E** to **G**) Magnified histological images of the sciatic nerve focusing on interfaces around the outer epineurium, comparing native tissue (E), adhesive interfaces (F), and nonadhesive interfaces (G). Dashed lines indicate the boundary of the outer epineurium. Scale bars, 100 μm. (**H**) Quantitative analysis of the outer epineurium thickness in diverse peripheral nerves. In the box plots, the center line indicates the mean, and whiskers represent the 5th and 95th percentiles of the data. Each experiment was repeated independently ($n = 8$ per group). Statistical significance and P values are determined by two-sided unpaired t test (NS, $^{*}P < 0.05$, $^{**}P < 0.01$, and $^{***}P < 0.001$).

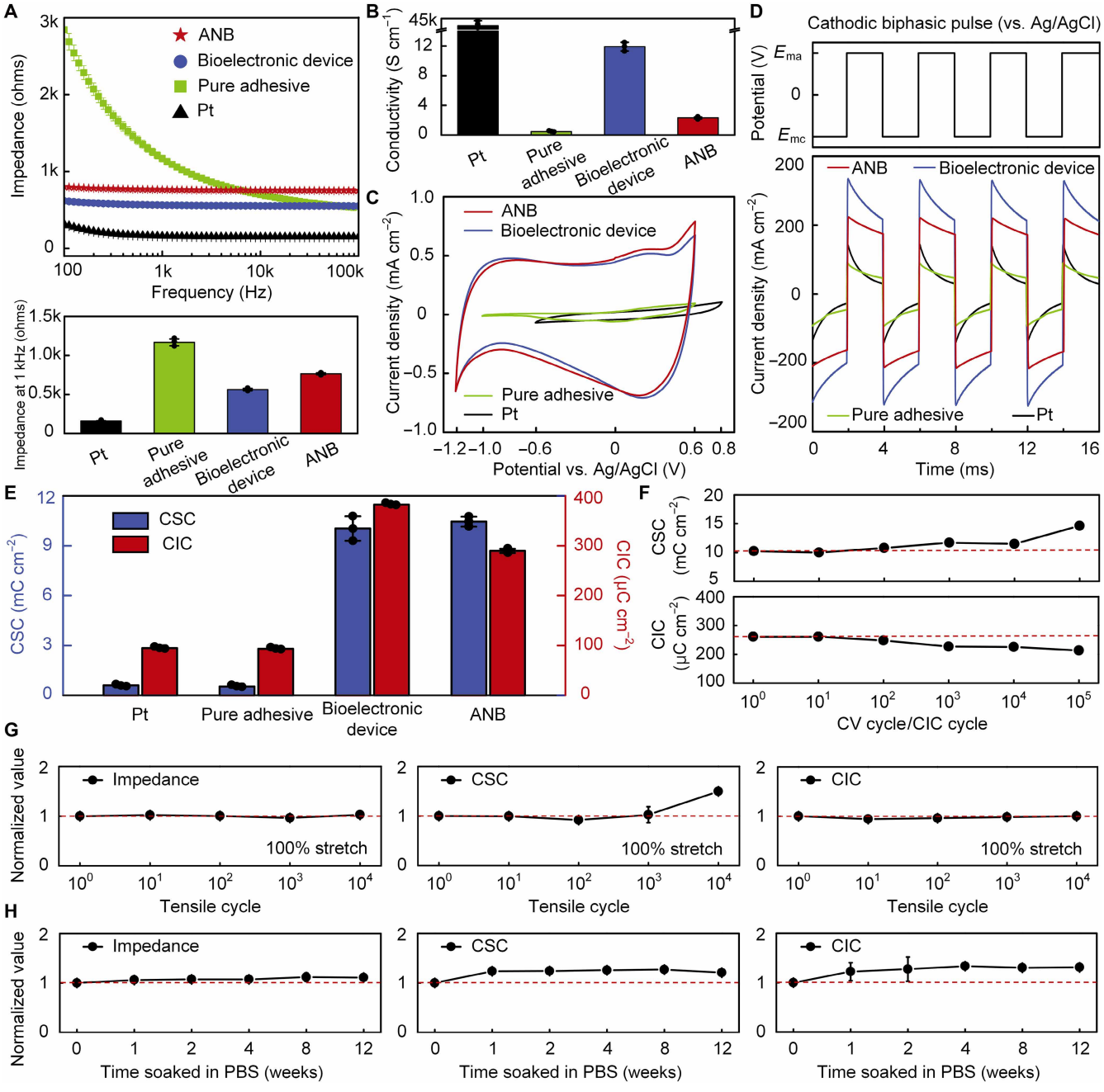

Fig. 3. Electrical properties and long-term stability of the ANB compared with the Pt electrode, the pure adhesive, and the bioelectronic device. (**A**) Impedance over a range of frequencies (top) and the corresponding impedance at 1 kHz (bottom). (**B**) Plots of electrical conductivity. (**C**) Current density as a function of applied potential with corrosion-resistant windows for each material. The details of corrosion-resistant windows are explained in fig. S14. (**D**) Current density induced by potential inputs according to cathodic biphasic pulse ranging maximum anodic potential (E_{ma}) to maximum cathodic potential (E_{mc}). (**E**) Resultant plots of CSC (left axis) and CIC (right axis) derived from plots (C) and (D), respectively. (**F**) CSC versus cyclic voltammetry cycles (top) and CIC versus CIC cycles (bottom) of the ANB. Red dashed lines indicate the initial value at the first cycle. Values in impedance, conductivity, CSC, and CIC represent the average and the SD (n = 3; independent samples). (**G**) Plots of impedance (left), CSC (middle), and CIC (right), normalized to the initial value at the first tensile cycle, as a function of the tensile cycle at 100% stretch. (**H**) Plots of impedance (left), CSC (middle), and CIC (right), normalized to the initial value before soaking in PBS solution, as a function of soaking time in PBS solution. Red dashed lines indicate the initial value at the first tensile cycle and before soaking in PBS solution. Values in impedance, CSC, and CIC represent the average and the SD ($n \geq 5$; independent samples).

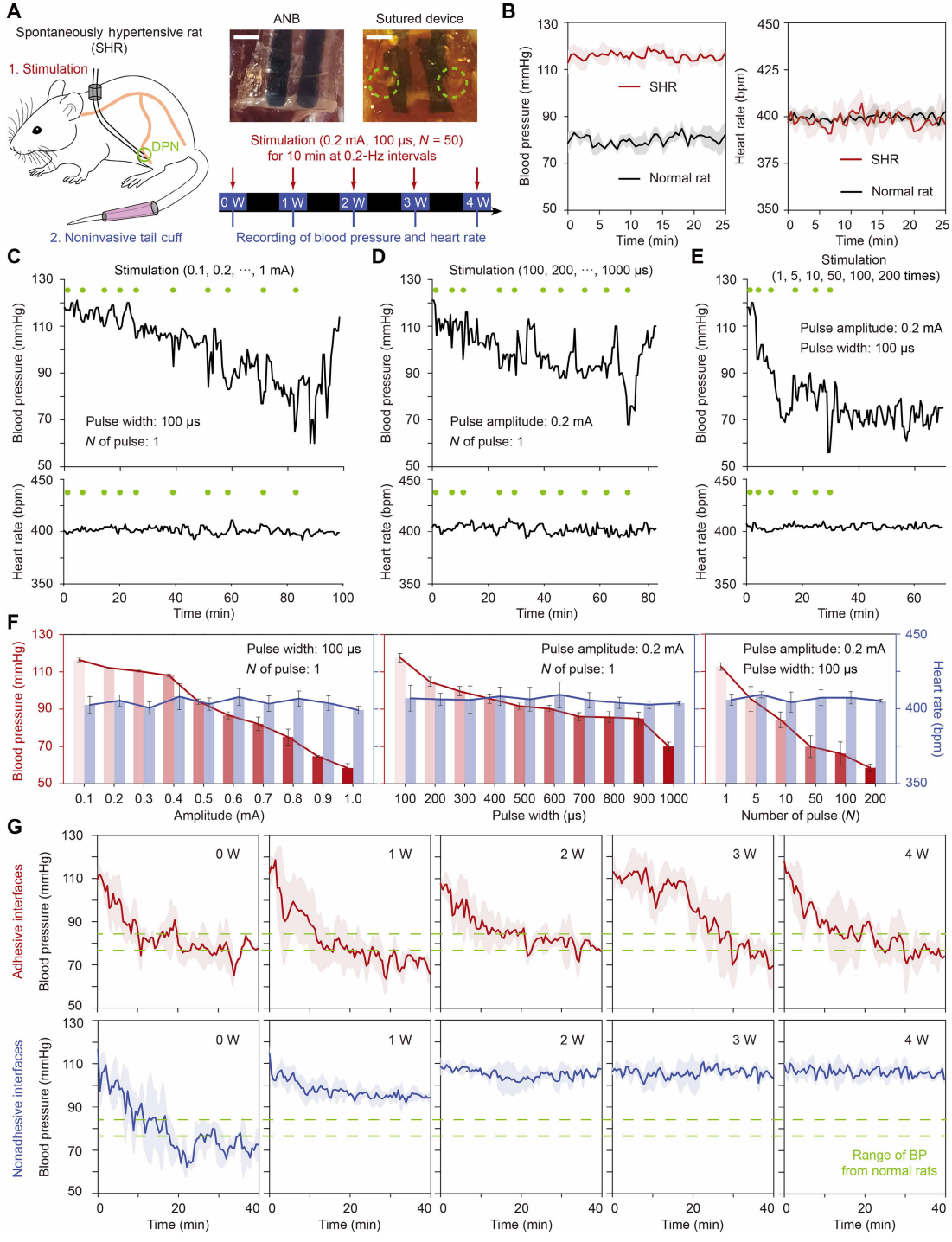

Fig. 4. BP regulation and HR changes upon DPN stimulation comparing adhesive interfaces and nonadhesive interfaces of bioelectronic devices. (**A**) Schematic illustration of the BP and HR measurement configuration under DPN stimulation using the ANB or the nonadhesive device in spontaneously hypertensive rats (SHR). Scale bars, 1 mm. W, weeks. (**B**) Plots depicting BP and HR without DPN stimulation comparing SHR and normal rats. (**C** to **E**) Characterization of BP regulation in SHR during DPN stimulation for three groups: current pulse changes in amplitude (0.1 to 1.0 mA; C), pulse width (100 to 1000 μs; D), and pulse number (1 to 200 pulses; E). The standard current pulse for DPN stimulation used an amplitude of 0.2 mA, a pulse width of 100 μs, and a pulse number of $N = 1$. Green dots indicate the timing of stimulation using different current pulses. Plots show continuous BP (top) and HR (bottom). (**F**) Plots of corresponding BP (red bar; left axis) and HR (blue bar; right axis) depending on DPN stimulations with various current pulses to characterize BP regulation. (**G**) Plots of continuous BP measured during long-term DPN stimulation over 4 weeks. Current pulses (0.2 mA, 100 μs, and $N = 50$) for 10 min at 0.2-Hz intervals were applied by the ANB with adhesive interfaces (red line; top) and the sutured device with nonadhesive interfaces (blue line; bottom). Green dashed lines denote the BP range (76 to 85 mmHg) in normal rats. Values in [(B), (F), and (G)] represent the mean and the SD, and each experiment was repeated independently ($n = 3$).

pronounced leg extension (movies S3 to S5). Specifically, BP decreased to 58, 70, and 58 mmHg when increasing the amplitude to 1.0 mA, the pulse width to 1000 μs, and the number of pulses to 200, respectively (Fig. 4F). Increasing the pulse amplitude above 0.4 mA resulted in a substantial BP decrease (Fig. 4F, left), whereas BP moderately declined upon increased pulse width (Fig. 4F, middle). This suggests that BP regulation through DPN stimulation is dominated by the pulse amplitude. However, when the pulse amplitude and width were increased from their base value (while maintaining $N = 1$), the BP returned to its initial high value only 10 min after the end of stimulation (Fig. 4, C and D). On the other hand, stimulation using $N = 50$ pulses or more—maintaining base amplitude and width parameters of 0.2 mA and 100 μs—allowed the BP of spontaneously hypertensive rats to remain similar to that of normal rats for more than 40 min after the end of stimulation (Fig. 4E). In all cases, the HR remained at ~400 bpm during DPN stimulation. On the basis of these results, we chose the stimulation parameters of current pulses to be 0.2 mA, 100 μs, and $N = 50$.

To demonstrate the long-term stimulation capability of our nonfibrotic interfaces, we compared the stimulation performance of two device groups: (i) the ANB with adhesive interfaces and (ii) the device with nonadhesive interfaces (Fig. 4G). Using the parameters derived above (0.2 mA, 100 μs, and $N = 50$), the ANB achieved BP regulation after 4 weeks of stimulation, reaching levels similar to normal rats (fig. S16A). The corresponding BP decreased by 34, 37, 33, 37, and 37% at 0 to 4 weeks, respectively (fig. S17A). These consistent values indicate that the effect of long-term adhesion of the ANB on the nerve was negligible for nerve conduction or stimulation quality. We observed negligible changes in HR during successful BP regulation with the ANB throughout 4 weeks, while a drop in HR is a known side effect of BP regulation using traditional methods (fig. S17B) (*49*, *50*). In contrast, the nonadhesive device managed to regulate BP only immediately after implantation (fig. S16B). Although stimulation 1 week after implantation yielded a slight BP decrease to 92 mmHg, the BP remained high relative to normal rat levels (76 to 85 mmHg). Overall, a significant decline in the stimulation performance was observed for the nonadhesive device, as the BP decreased by 40, 16, 3, 2, and 2% at 0 to 4 weeks, respectively (fig. S17A).

Immunofluorescence analysis post–nerve stimulation

To further validate the long-term antifibrotic performance of our adhesive bioelectronic interface, we conducted an immunofluorescence analysis on DPN samples actuated once a week for 4 weeks and collected 12 weeks after implantation. As previously, we compared native tissue (Fig. 5A), the ANB (Fig. 5B), and the nonadhesive device (Fig. 5C).

The nonadhesive interface showed a 28% reduced neurofilament density compared to that of native tissue (Fig. 5D). Notably, in the images of the magnified epineurium interface (fig. S18A), the nonadhesive device showed not only sparse neurofilaments but also contracted nerve fascicles—hallmarks of functional loss and sustained inflammation. In addition, we observed significant macrophage (CD68) infiltration in the nerve itself for the nonadhesive implant, with a 45% increase from native tissue (Fig. 5E and fig. S18B). Similarly, angiogenesis was stronger around the nonadhesive device as shown by a 56% higher blood vessel density compared to native tissue [α-smooth muscle actin (α-SMA)] throughout the nerve epineurium and fibrous capsule (Fig. 5F). We also detected fibroblast activity throughout the nerve epineurium and fibrous capsule, indicative of a chronic fibrotic response (fig. S18C). In turn, fibroblasts induced substantial type-I collagen (Col-I) deposition at the epineurium and fibrous capsule (Fig. 5G). These factors led to major thickening of the epineurium of nonadhesive interfaces, which reached more than three times the thickness of the adhesive interfaces (fig. S18D). In contrast, the DPN implanted with our ANB exhibited a neurofilament density comparable to that of native tissue (Fig. 5, B and D). The DPN-ANB interface closely resembled native tissue across all evaluated metrics (Fig. 5, D to F). In particular, no macrophage infiltration in the nerve and adhesive interface was observed across all samples (Fig. 5E and fig. S18B). There was also no detectable fibroblast activity or fibrotic collagen deposition around the nerve, and the collagen thickness remained comparable to native tissue (Fig. 5F).

To further examine the temporal progression of inflammation underlying the functional decline of nonadhesive interfaces, we monitored the response during the first 4 weeks of device implantation on the DPN (fig. S19). As early as 1 day postimplantation, abundant macrophages initiated a foreign body response around the epineurium. By week 1, a densely cellularized collagen-rich fibrous capsule had formed, corresponding with the observed loss of stimulation capability. Neurofilament density began to markedly decrease by week 2, while macrophages progressively infiltrated the nerve through the epineurium from week 3 onward. Fibroblast activity within the fibrous capsule increased up to week 2 and then gradually declined.

DISCUSSION

Using our adhesive bioelectronic device ensures the formation of a nonfibrotic interface and enables long-term and stable implantation on various peripheral nerves. This study builds on our previously reported adhesive antifibrotic patch (*47*), which suppressed fibrosis on organ surfaces but did not provide functional neuromodulation. Here, we introduce a fully integrated ANB system tailored for peripheral nerves. By combining adhesive hydrogel chemistry with multimaterial 3D printing of insulating and conductive layers, we created a customizable electrode architecture capable of stable long-term neuromodulation.

Although many strategies for device implantation have emerged to secure contact with peripheral nerves—such as soft-actuating (*51*), nanoclip (*52*), shape memory (*53*), and self-healing (*3*, *54*) devices—these physical contact methods still impose mechanical pressure. A constant pressure below 4 kPa is recommended for chronic implantation on peripheral nerves to prevent nerve function degradation (*55*). However, this criterion is hard to achieve with these nonadhesive methods because electrical recording or stimulation requires constant contact with the bioelectronic devices through external pressure. In contrast, robust electrical contact with the ANB does not rely on such pressure. We highlight that although peripheral nerves are generally considered less immunogenic than many other tissues, fibrosis at nerve-device interfaces is still common. This response arises largely from mechanical micromotion in the dynamic implantation environment, rather than from material surface chemistry (*56*). By covalently anchoring the interface and suppressing micromotion, the ANB prevents the chronic irritation that would otherwise drive fibrotic encapsulation.

The mechanical and electrical characterization of the ANB showed that it exhibits properties of high softness, stretchability, and interfacial toughness desirable for in vivo implantation. In addition,

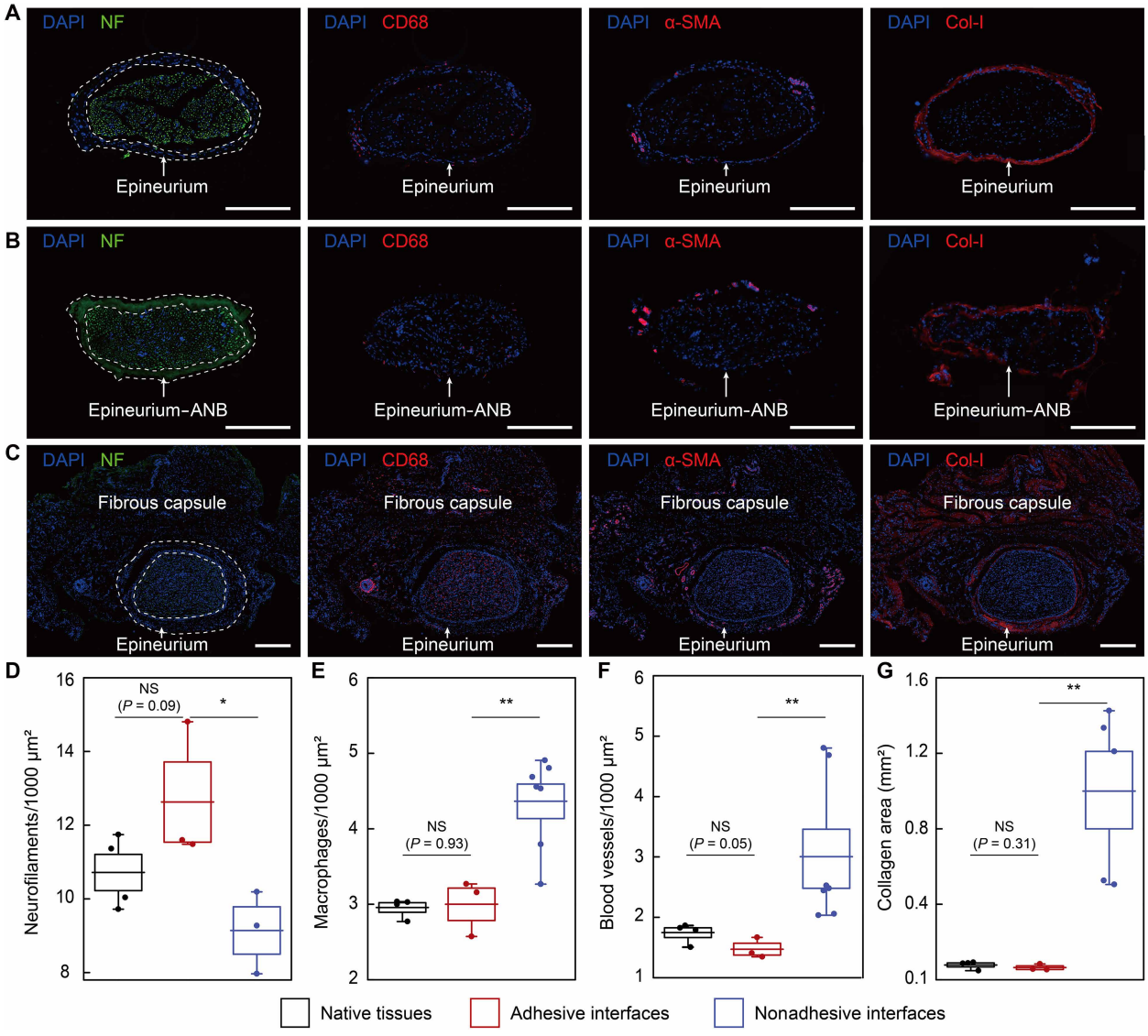

Fig. 5. Immunofluorescence images of the DPN post–nerve stimulation. (**A** to **C**) Neurofilament (NF; green), macrophages (CD68; red), α-smooth muscle actin (α-SMA; red), type-I collagen (Col-I; red), and nuclei [4′,6-diamidino-2-phenylindole (DAPI); blue] are compared in native tissue (A), adhesive interfaces after 12 weeks of implantation of the ANB (B), and nonadhesive interfaces after 12 weeks of implantation of the nonadhesive device (C). NF, CD68, α-SMA, Col-I, and DAPI represent markers for nerve fascicles, macrophages, blood vessels, collagen, and cell nuclei, respectively. Dashed lines and arrows indicate the area of epineurium for native tissue and nonadhesive interfaces and epineurium-ANB for adhesive interfaces. Fibrous capsules are observed at the nonadhesive interfaces. Scale bars, 200 µm. (**D** to **F**) Quantitative analysis of the immunofluorescence results. The number of NFs (D), macrophages (E), and blood vessels (G) per 1000 μm^2 and the total collagen area (F) are compared in native tissue (black), adhesive interfaces (red), and nonadhesive interfaces (blue). Each experiment was repeated independently ($n \geq 3$ per group). Statistical significance and *P* values are determined by two-sided unpaired *t* test (NS, $*P < 0.05$, and $**P < 0.01$).

we verified that the ANB remains mechanically and electrically stable for long term in vivo use, showing robust stimulation performance after 100,000 tensile cycles to 100% stretch, 10,000 CSC/CIC cycles, and 12 weeks of PBS immersion at RT. In addition, the bioadhesive hydrogel in direct contact with nerves is ultrasoft and highly stretchable, fulfilling biocompatibility requirements (*27*) and preventing the occurrence of mechanically driven FBR (*43*). We also proved that the adhesion of the ANB ensures nonfibrotic interfaces on peripheral nerves after 12 weeks of device implantation.

In past studies, BP has been regulated by stimulating the carotid sinus or vagus nerve, both of which play an important role in metabolism, such as regulating hypertension, glucose level, and breathing rate (*57*–*60*). However, stimulation of these targets can cause side effects such as HR decreases, apnea, cough, and paresthesia (*61*–*63*). To demonstrate the unprecedented capabilities unlocked by our ANB, we confirmed long-term BP regulation in vivo by a 37% decrease in BP after DPN stimulation of a spontaneously hypertensive rat model for up to 4 weeks. This regulation was achieved without the undesirable HR decrease observed in existing methods. In contrast, nonadhesive bioelectronic interfaces lost most of their performance 1 week only after the implantation of the device because a thick fibrous capsule formed at the interface, limiting

electrical contact. These results are consistent with findings from histological and immunofluorescence analysis of peripheral nerves collected after implantation. The nonadhesive device showed thick fibrous encapsulation around the nerve and reduced neurofilament density, which are signs of chronic inflammation and functional loss. On the other hand, our adhesive interfaces were comparable to native nerve tissue for all biological metrics considered. In summary, DPN stimulation using nonfibrotic interfaces is a promising solution for long-term BP regulation without causing the HR to decrease. Beyond the fixed biphasic parameters used here, future work will explore waveform optimization (e.g., pulse shape, interphase gap, and frequency) to enhance neural selectivity and minimize off-target effects. Overall, we envision that adhesive bioelectronic interfaces will provide a robust strategy for long-term, nonfibrotic device integration while also opening promising avenues for translational efforts in bioelectronics-based disease treatment, rehabilitation, and human augmentation.

MATERIALS AND METHODS

Materials

For the preparation of the insulating layer, low–water content PU (HydroThane AL-25 80A, AdvanSource Biomaterials), dimethylformamide (DMF) (Sigma-Aldrich), and tetrahydrofuran (THF) (Sigma-Aldrich) were used. For the preparation of the conductive hydrogel, PEDOT:PSS solution (Clevios PH 1000, Heraeus Electronic Materials), dimethyl sulfoxide (DMSO; Sigma-Aldrich), ethanol (Sigma-Aldrich), and hydrophilic PU (HydroMed D3, AdvanSource Biomaterials) were used. For the preparation of the bioadhesive hydrogel, acrylic acid (Sigma-Aldrich), a PVA [molecular weight (M_w) of 146,000 to 186,000 and 99+% hydrolyzed; Sigma-Aldrich], hydrophilic PU (HydroMed D3, AdvanSource Biomaterials), α-ketoglutaric acid (Sigma-Aldrich), poly(ethylene glycol) dimethacrylate (PEGDMA) (Sigma-Aldrich), and NHS (Sigma-Aldrich) were used. For 3D printing onto a glass substrate, a PVA (M_w of 31,000 to 50,000 and 87 to 89% hydrolyzed; Sigma-Aldrich), Nozzles (100 and 200 μm; Nordson EFD) and a 5-ml syringe (Nordson EFD) were used. The porcine skin and muscle tissue used for adhesion tests were purchased from a research-grade biological tissue vendor (Sierra Medical Inc.).

Preparation of the insulating layer

To prepare the insulating layer, a low–water content PU was prepared after drying overnight in a 40°C oven. We dissolved the dried low–water content PU in a solvent solution [DMF:THF = 1:1 (v/v)] at a concentration of 25 w/w % for 24 hours.

Preparation of the conductive hydrogel

A PEDOT:PSS solution was mixed for 6 hours at RT and was filtered through a nylon syringe filter (0.45-μm pores; Tisch Scientific). The filtered solution was cryogenically dried using a freeze dryer (FreeZone, Labconco) for 72 hours. The lyophilized PEDOT:PSS was dissolved in a solution [deionized water:DMSO = 85:15 (v/v)] at a concentration of 7 w/w %. This mixture was homogeneously blended by a mortar grinder (RM 200, Retch). Meanwhile, a hydrophilic PU was prepared after drying overnight in a 40°C oven. The dried hydrophilic PU was diluted with a 70% ethanol solution to a concentration of 10 w/w %. The blended PEDOT:PSS and the 10 w/w % hydrophilic PU were mixed in a 2:1 (v/v) ratio for 1 hour at RT, followed by consecutive filtering with polypropylene syringe filters (20- and 10-μm pores; Tisch Scientific). The conductive hydrogel was synthesized using a previously reported method (*45*).

Preparation of the bioadhesive hydrogel

A precursor solution was prepared by mixing 32 w/w % acrylic acid, 7 w/w % PVA, 0.2 w/w % α-ketoglutaric acid, and 0.05 w/w % PEGDMA with deionized water and then dissolving 30 mg of NHS in each 1 ml of the mixed solution (fig. S3). The precursor solution was transferred into a transparent mold with a thickness of 70 μm and cured in an ultraviolet (UV) chamber (365 nm and 0.4 mW/cm^2) for 30 min. The bioadhesive hydrogel was synthesized using a previously reported method (*46*, *47*).

Fabrication of the ANB

A sacrificial layer of a PVA (20 w/w % in deionized water) was spin coated on a glass substrate at 500 rpm for 1 min and dried at 70°C for 1 hour. To fabricate the bioelectronic device, the insulating layer, the conductive hydrogel, and another insulating layer were consecutively patterned by a customized 3D printer using a Cartesian gantry system (AGS1000, Aerotech) and a liquid dispenser system (Ultimus V, Nordson EFD). We used nozzles of 100 and 200 μm for printing the conductive hydrogel and the insulating layer, respectively. In addition, we applied extruding pressures of 90 and 280 kPa to print the conductive hydrogel and the insulating layer, respectively. The pattern pathways were designed with AutoCAD (Autodesk) and converted into G-code via CADFusion (Aerotech) to command the *X*-*Y*-*Z* motion of the print head. This direct ink writing approach reliably achieved a minimum line width of ~100 μm, consistent with the nozzle dimensions and rheological properties of the inks. The patterned bioelectronic device was lifted from the glass substrate by immersing it in deionized water for 10 min. This bioelectronic device was attached to the UV-cured bioadhesive hydrogel and dried in a fume hood with airflow under ambient conditions for 12 hours. Before implantation on peripheral nerves, the fabricated ANB was prepared using aseptic techniques and disinfected under UV-C light (254 nm) for 30 min.

In vitro NHS ester activity

To confirm NHS ester reactivity, hydrogel bioadhesive samples were incubated with a primary amine probe. Dry hydrogel samples were immersed in a 50 μM solution of Alexa Fluor 488–cadaverine (Invitrogen) in PBS (pH 7.4) for 30 min at RT. Samples were then washed five times with 10% ethanol in PBS (5 min each), followed by a final PBS rinse. As a negative control, hydrogel samples preincubated in PBS overnight to deactivate NHS esters were processed in parallel. Samples were imaged on a confocal microscope (SP8, Leica; 5× objective) using excitation/emission at 493/516 nm under identical acquisition settings. Fluorescence intensity was quantified in ImageJ as mean intensity per unit sample area.

In vitro biocompatibility

We performed in vitro biocompatibility experiments to assess the cytotoxicity of the adhesive hydrogel and PU layers directly in contact with the nerve's surface. Dry hydrogel-PU thin films (10 mg/ml), UV-sterilized before use, were incubated in Dulbecco's modified Eagle's medium (DMEM; Gibco) supplemented with 10% (v/v) fetal bovine serum and 1% (v/v) penicillin-streptomycin at 37°C for 24 hours to prepare conditioned medium. BALB/c 3T3 mouse embryonic fibroblasts (American Type Culture Collection, CCL-163) were

cultured under standard conditions (37°C and 5% CO_2) and exposed to hydrogel-PU–conditioned medium for 24 hours. Pristine-supplemented DMEM was used as the control. Cell viability was determined using a LIVE/DEAD cell imaging kit (Invitrogen) and following the manufacturer's protocol. Cells were imaged on a confocal microscope (SP8, Leica; 5× objective) to image live cells with excitation/emission at 488/515 nm (live), and 570/602 nm (dead). Cell viability was quantified in ImageJ by counting live and dead cells.

Mechanical characterizations

To measure the interfacial toughness of the bioadhesive hydrogel, adhesion tests were performed using a standard T-peeling test (ASTM F2256) using a universal testing machine (2.5-kN load cell; zwickiLine Z2.5, Zwick/Roell). Porcine skin and muscle were prepared by washing them with PBS. A polyimide film (thickness of 50 μm; Goodfellow) was bonded to the bioadhesive hydrogel as a stiff backing with cyanoacrylate glue (Krazy Glue). This bioadhesive hydrogel (10 mm in width) was attached to biological tissue with gentle pressure for 5 s, and then one side of the sample was pulled at a speed of 300 μm s^{-1}. The measured force reached a plateau, as the peeling process entered a steady state (fig. S6). Interfacial toughness was calculated by dividing the plateau force by twice the width of the tissue sample. For the accelerated aging experiment, the ANB (without PEDOT:PSS) was adhered to porcine muscle tissue. The ANB-muscle sample was placed in a 95% relative humidity chamber at 45°C for 20 days, equivalent to an aging time of up to 12 weeks according to the ASTM F1980 accelerated aging test standard.

For measurement of Young's modulus, maximum stretch, and tensile strength, we conducted a standard tensile test (ASTM D412), using three groups: the pure bioadhesive (4 to 7 mm in width, 3 to 6 mm in length, and 100 μm in thickness), the bioelectronic device (4 mm in width, 4 mm in length, and 50 μm in thickness), and the ANB (4 mm in width, 4 mm in length, and 150 μm in thickness). All samples were prepared in a swollen state after being immersed in PBS for 3 hours. Both sides of the samples were clamped, and one side was pulled by a materials testing machine (4.4-N load cell; UStretch, CellScale), measuring the corresponding force. The resulting stress-strain curves were used to determine Young's modulus, maximum stretch, and tensile strength (fig. S10). Notably, Young's modulus was defined as the initial slope of the stress-strain curve. Maximum stretch and tensile strength were measured at the point of sample rupture.

Electrical characterizations

For electrical characterizations, we compared the Pt electrode (40 mm in width, 40 mm in length, and 25 μm in thickness), the pure adhesive (40 mm in width, 40 mm in length, and 100 μm in thickness), the bioelectronic device (0.7 mm in width, 2 mm in length, and 50 μm in thickness), and the ANB (0.7 mm in width, 2 mm in length, and 150 μm in thickness) in conductivity, impedance, CSC, and CIC. All samples were prepared in a swollen state after being immersed in PBS for 3 hours. The sheet resistance of samples was measured by a standard four-point probe (4200-SCS, Keithley), and the electrical conductivity was calculated as

$$\sigma = \frac{L}{R \times W \times T} \tag{1}$$

where σ is electrical conductivity, L is the distance between the two electrodes for voltage measurement, R is the sheet resistance, W is the sample width, and T is the sample thickness.

Electrochemical impedance spectroscopy was conducted using a potentiostat/galvanostat (Autolab IMP, Metrohm) to measure impedance, CSC, and CIC. A three-electrode configuration was used: the sample as the working electrode, a Pt wire electrode as the counter electrode, and an Ag/AgCl electrode as the reference electrode. These electrodes were immersed in PBS (pH 7.4) inside a Faraday cage. Impedance was measured from 10 Hz to 100 kHz with a bias of 10 mV versus Ag/AgCl. Meanwhile, the corrosion-resistant window of each sample was acquired by applying a biphasic current pulse (±0.7 mA in amplitude, 2 ms in pulse width, and 0.5 ms in interphase gap) (fig. S14). From the corresponding potential of each sample, window limits (from E_{mc} to E_{ma}) were measured as

$$\begin{aligned} E_{mc} &= V_{mc} - |V_{access}| \\ E_{ma} &= V_{ma} - |V_{access}| \end{aligned} \tag{2}$$

where E_{mc} is the maximum cathodic potential, V_{mc} is the maximum cathodic voltage transient, V_{access} is the access voltage, E_{ma} is the maximum anodic potential, and V_{ma} is the maximum anodic voltage transient.

Cyclic voltammetry measurements were performed to calculate CSC at a scan rate of 100 mV/s within the corrosion-resistant window of each sample. In contrast, current density measurements were conducted to calculate CIC by applying a biphasic potential pulse (E_{mc} – E_{ma} in amplitude and 2 ms in pulse width). The CSC was calculated from the cyclic voltammetry curves, and the CIC was calculated from the current density transient as

$$\mathrm{CSC} = \frac{1}{\nu} \int_{Ec}^{Ea} |J| dE \tag{3}$$

where ν is the scan rate, E_a is the potential limit of the anode, E_c is the potential limit of the cathode, J is the measured current density, and E is the potential versus Ag/AgCl.

$$\mathrm{CIC} = \frac{Q_{inj(c)} + Q_{inj(a)}}{A} \tag{4}$$

where $Q_{inj(c)}$ is the total injected charge in the cathodic phase, $Q_{inj(a)}$ is the total injected charge in the anodic phase, and A is the sample area.

In vivo ANB implantation on diverse peripheral nerves

All animal studies in rats were approved by the Committee on Animal Care (protocol number: 2209000422) at the Massachusetts Institute of Technology (MIT), and all surgical procedures and postoperative care were supervised by the MIT Division of Comparative Medicine veterinary staff. The animal care and use programs at MIT meet the requirements of Federal Law (89-544 and 91-579) and NIH regulations and are also accredited by the American Association for Accreditation of Laboratory Animal Care International. SD rats (female and male, 200 to 250 g, 10 weeks; Charles River Laboratories) and spontaneously hypertensive rats (female and male, 150 to 180 g, 8 weeks; Charles River Laboratories) were used for all in vivo rat studies. All samples were prepared using aseptic techniques and further sterilized under UV light (254 nm) for 30 min before implantation.

For implantation of the ANB on diverse peripheral nerves, animals were anesthetized with inhaled isoflurane (2 to 3% isoflurane

in oxygen) in an anesthesia chamber. They were then placed on a heating pad, and anesthesia was maintained at 2% isoflurane via a nose cone throughout the surgery. Respiratory rate and breathing quality were continuously monitored to confirm anesthesia depth. Buprenorphine SR was injected subcutaneously at 1.0 mg/kg for analgesia. We then applied eye ointment to prevent corneal irritation, and hair at the incision site was shaved, followed by sterilization with betadine and 70% ethanol. A 2-cm incision was made in the dermis over the locations of the target nerves: the central head near the right ear for the occipital nerve, the ventral side of the neck over the jugular vein for the vagus nerve, the fibula side of the leg for the DPN, and the femur side of the leg for the sciatic nerve, tibial nerve, and common peroneal nerve. These nerves were exposed by separating the muscles from the fascia layer on the outer epineurium of nerves. The ANB for adhesive interfaces and the sutured device for nonadhesive interfaces ($n = 8$ for each nerve) were implanted on the nerve surface. The nonadhesive device was prepared by immersing the ANB in PBS for 3 hours before implantation. Devices were wrapped around their nerve for the implantation. The ANB adhered to the nerve, whereas the nonadhesive device was secured with sutures (6-0 Silk, Ethicon) to the nerve-surrounding substrates of the device itself. Next, the incision was closed with sutures (5-0 Vicryl, Ethicon), and 4 ml of warm saline were injected subcutaneously to prevent dehydration. For BP regulation studies, the ANB and the sutured device were implanted on the DPN of the spontaneously hypertensive rat model. An additional 2-cm incision was made at the animals' cervical region, and the electric wires of the implanted device were tunneled subcutaneously from the DPN to the cervical region under the skin. In addition, a pedestal port was implanted in the cervical incision site and fixed when closed with sutures (5-0 Nylon, Ethicon). The wires were placed inside the pedestal port to store them after the animals woke from anesthesia. The ANB fully functioned throughout the study period, and the endpoint of the study was determined for investigational purposes rather than by implant failure. All animals in the study survived and were kept in normal health conditions based on daily monitoring by the MIT Division of Comparative Medicine veterinarian staff. At the end of the study, animals were euthanized through CO_2 inhalation.

Histology

All peripheral nerves with bioelectronic device implantation were collected after euthanasia and fixed in a 10% formalin solution for 24 hours. The fixed nerves were stored in 70% ethanol and submitted for paraffin embedding at the Hope Babette Tang (1983) Histology Facility of the Koch Institute for Integrative Cancer Research at MIT. The paraffin block–embedded nerve samples were sectioned in a thickness of 4 μm and stained with H&E and MT. The H&E and MT slides were scanned using a digital slide scanner (Aperio, Leica). All histological assessments of the randomly mixed nerve samples were performed in a blinded manner by pathologists who were unaware of the study group assignments.

In vivo BP regulation without HR change

For BP and HR measurements, SD rats and spontaneously hypertensive rats implanted with bioelectronic devices and pedestal ports were anesthetized using 1.5% inhaled isoflurane. SD rats were used as a control to represent the rat model in a normal state. A noninvasive tail cuff was placed on the tail of the animals, and both BP and HR were measured using a commercial BP monitoring system (CODA Monitor, Kent Scientific). To stimulate DPN for BP regulation, electrodes of the ANB or the sutured device were implanted in spontaneously hypertensive rats and were connected to a RHS Stim/Recording Controller (Intan Technologies). For BP regulation characterization in spontaneously hypertensive rats, a current pulse (0.2 mA in amplitude and 100 μs in pulse width) was the standard for DPN stimulation. We measured the BP and HR upon DPN stimulation with different current pulses by varying amplitude (0.1 to 1.0 mA), pulse width (100 to 1000 μs), and pulse number (1 to 200 pulses). To demonstrate long-term BP regulation, we stimulated DPN with current pulses (0.2 mA in amplitude, 100 μs in pulse width, and $N = 50$ pulses) for 10 min at 0.2 Hz.

Immunofluorescence

The DPN was harvested from spontaneously hypertensive rats 8 weeks poststimulation in three groups: native tissue, the ANB implantation, and the sutured device implantation. The sample was fixed overnight in a 10% formalin solution and then immersed in 15 and 30% sucrose solutions (in PBS) for 4 hours and overnight, respectively. Then, the sample was embedded in the optimal cutting temperature (OCT) compound (Tissue-Tek, Sakura Finetek USA) and frozen in a dry ice-ethanol container at −78°C. The sample embedded in a frozen OCT compound block was sliced using a cryostat (Shandon Cryotome, Thermo Fisher Scientific) with a 12-μm thickness. For immunofluorescence staining, tissue slides were washed three times in a wash buffer solution (0.3% Triton X-100 in PBS) for 5 min each. Next, they were incubated with a blocking solution (10% normal donkey serum in wash buffer solution) for 1 hour at RT. Then, the samples were incubated overnight at 4°C with primary antibodies in a diluent solution (5% normal donkey serum in wash buffer solution): mouse anti-NF200 (1:200; N5389, Sigma-Aldrich), rabbit anti-CD68 (1:500; ab125212, Abcam), rabbit anti-α-SMA (1:100; ab5694, Abcam), rabbit anti–Collagen I (1:100; ab316222, Abcam), and goat anti–Collagen I (1:100; catalog no. 1310-01, SouthernBiotech). For α-SMA immunolabeling, permeabilization was performed using 2% Triton X-100 in PBS for 30 min at RT before primary antibody treatment. Next, the sample was rinsed three times for 5 min each using the wash buffer solution, followed by incubation with secondary antibodies in the diluent solution for 2 hours at RT: Alexa Fluor 488–conjugated goat anti-mouse (1:1000; ab150113, Abcam), Alexa Fluor 488–conjugated donkey anti-goat (1:1000; ab150129, Abcam), and Alexa Fluor 647–conjugated donkey anti-rabbit (1:1000; ab150075, Abcam). Next, the samples were rinsed three times for 5 min each using the wash buffer solution, followed by nuclear counterstaining performed using 4′,6-diamidino-2-phenylindole (DAPI) (1:1000; catalog no. 62248, Thermo Fisher Scientific). The samples were washed three times for 5 min each with PBS and were then coverslipped using a ProLong glass antifade mounting medium (catalog no. P36980, Invitrogen). After curing the mounted sample at RT for 12 hours, fluorescent images were acquired using a fluorescent slide scanner system and a 20× objective (TissueFAXS SL, TissueGnostics). The density of nerve fascicles, macrophages, and blood vessels and the fluorescent area of collagen were quantified using an image analysis software (v0.5.1; QuPath). We expressed the density of a particular marker as the number of the positive cells/structures per 1000 μm^2. All analyses were performed blinded with respect to the experimental conditions.

Statistical analysis

All data obtained from this study were presented as the mean ± SD unless otherwise stated. MATLAB (R2021b, MathWorks) was used to assess the statistical significance in all comparisons in this study. In the statistical analysis for comparison between two data groups, the two-tailed unpaired *t* test was used. The significance levels were NS (not significant), $*P < 0.05$, $**P \leq 0.01$, and $***P \leq 0.001$.

Supplementary Materials

The PDF file includes:
Figs. S1 to S19
Legends for movies S1 to S5

Other Supplementary Material for this manuscript includes the following:
Movies S1 to S5

REFERENCES AND NOTES

1. M. Silvera Ejneby, M. Jakesova, J. J. Ferrero, L. Migliaccio, I. Sahalianov, Z. Zhao, M. Berggren, D. Khodagholy, V. Derek, J. N. Gelinas, E. D. Glowacki, Chronic electrical stimulation of peripheral nerves via deep-red light transduced by an implanted organic photocapacitor. *Nat. Biomed. Eng.* **6**, 741–753 (2022).
2. J. C. Chen, P. Kan, Z. Yu, F. Alrashdan, R. Garcia, A. Singer, C. S. E. Lai, B. Avants, S. Crosby, Z. Li, B. Wang, M. M. Felicella, A. Robledo, A. V. Peterchev, S. M. Goetz, J. D. Hartgerink, S. A. Sheth, K. Yang, J. T. Robinson, A wireless millimetric magnetoelectric implant for the endovascular stimulation of peripheral nerves. *Nat. Biomed. Eng.* **6**, 706–716 (2022).
3. Y. Liu, J. Li, S. Song, J. Kang, Y. Tsao, S. Chen, V. Mottini, K. McConnell, W. Xu, Y. Q. Zheng, J. B. Tok, P. M. George, Z. Bao, Morphing electronics enable neuromodulation in growing tissue. *Nat. Biotechnol.* **38**, 1031–1036 (2020).
4. R. Tao, B. Mi, Y. Hu, S. Lin, Y. Xiong, X. Lu, A. C. Panayi, G. Li, G. Liu, Hallmarks of peripheral nerve function in bone regeneration. *Bone. Res.* **11**, 6 (2023).
5. S. Das, W. J. Gordian-Velez, H. C. Ledebur, F. Mourkioti, P. Rompolas, H. I. Chen, M. D. Serruya, D. K. Cullen, Innervation: The missing link for biofabricated tissues and organs. *NPJ Regen. Med.* **5**, 11 (2020).
6. M. D. Ferrari, P. J. Goadsby, R. Burstein, T. Kurth, C. Ayata, A. Charles, M. Ashina, A. van den Maagdenberg, D. W. Dodick, Migraine. *Nat. Rev. Dis. Primers.* **8**, 2 (2022).
7. L. A. Wilbrink, I. F. de Coo, P. G. G. Doesborg, W. M. Mulleners, O. P. M. Teernstra, E. C. Bartels, K. Burger, F. Wille, R. T. M. van Dongen, E. Kurt, G. H. Spincemaille, J. Haan, E. W. van Zwet, F. Huygen, M. D. Ferrari, I. s. group, Safety and efficacy of occipital nerve stimulation for attack prevention in medically intractable chronic cluster headache (ICON): A randomised, double-blind, multicentre, phase 3, electrical dose-controlled trial. *Lancet Neurol.* **20**, 515–525 (2021).
8. N. D. Engineer, T. J. Kimberley, C. N. Prudente, J. Dawson, W. B. Tarver, S. A. Hays, Targeted vagus nerve stimulation for rehabilitation after stroke. *Front. Neurosci.* **13**, 280 (2019).
9. J. Dawson, C. Y. Liu, G. E. Francisco, S. C. Cramer, S. L. Wolf, A. Dixit, J. Alexander, R. Ali, B. L. Brown, W. Feng, L. DeMark, L. R. Hochberg, S. A. Kautz, A. Majid, M. W. O'Dell, D. Pierce, C. N. Prudente, J. Redgrave, D. L. Turner, N. D. Engineer, T. J. Kimberley, Vagus nerve stimulation paired with rehabilitation for upper limb motor function after ischaemic stroke (VNS-REHAB): A randomised, blinded, pivotal, device trial. *Lancet* **397**, 1545–1553 (2021).
10. P. Dugan, O. Devinsky, Epilepsy: Guidelines on vagus nerve stimulation for epilepsy. *Nat. Rev. Neurol.* **9**, 611–612 (2013).
11. The Vagus Nerve Stimulation Study, A randomized controlled trial of chronic vagus nerve stimulation for treatment of medically intractable seizures. *Neurology* **45**, 224–230 (1995).
12. L. Y. Kamel, W. Xiong, B. M. Gott, A. Kumar, C. R. Conway, Vagus nerve stimulation: An update on a novel treatment for treatment-resistant depression. *J. Neurol. Sci.* **434**, 120171 (2022).
13. S. Raspopovic, G. Valle, F. M. Petrini, Sensory feedback for limb prostheses in amputees. *Nat. Mater.* **20**, 925–939 (2021).
14. F. M. Petrini, M. Bumbasirevic, G. Valle, V. Ilic, P. Mijovic, P. Cvancara, F. Barberi, N. Katic, D. Bortolotti, D. Andreu, K. Lechler, A. Lesic, S. Mazic, B. Mijovic, D. Guiraud, T. Stieglitz, A. Alexandersson, S. Micera, S. Raspopovic, Sensory feedback restoration in leg amputees improves walking speed, metabolic cost and phantom pain. *Nat. Med.* **25**, 1356–1363 (2019).
15. R. Cartwright, V. Khullar, Clinical trials: Percutaneous tibial nerve stimulation for overactive bladder. *Nat. Rev. Urol.* **7**, 181–182 (2010).
16. A. Fenner, eCoin device stops patients from spending a penny. *Nat. Rev. Urol.* **16**, 2 (2019).
17. Y.-t. Kim, A. Kanneganti, C. Nothnagle, R. Landrith, M. Mizuno, M. B. J. Wijesundara, S. Smith, M. I. Romero-Ortega, Microchannel electrode stimulation of deep peroneal nerve fascicles induced mean arterial depressor response in hypertensive rats. *Bioelectron. Med.* **2**, 55–62 (2015).
18. R. Feiner, T. Dvir, Tissue–electronics interfaces: From implantable devices to engineered tissues. *Nat. Rev. Mater.* **3**, 17076 (2018).
19. J. W. Salatino, K. A. Ludwig, T. D. Y. Kozai, E. K. Purcell, Glial responses to implanted electrodes in the brain. *Nat. Biomed. Eng.* **1**, 862–877 (2017).
20. D. G. Barone, A. Carnicer-Lombarte, P. Tourlomousis, R. S. Hamilton, M. Prater, A. L. Rutz, I. B. Dimov, G. G. Malliaras, S. P. Lacour, A. A. B. Robertson, K. Franze, J. W. Fawcett, C. E. Bryant, Prevention of the foreign body response to implantable medical devices by inflammasome inhibition. *Proc. Natl. Acad. Sci. U.S.A.* **119**, e2115857119 (2022).
21. J. S. Duffield, M. Lupher, V. J. Thannickal, T. A. Wynn, Host responses in tissue repair and fibrosis. *Annu. Rev. Pathol.* **8**, 241–276 (2013).
22. A. Carnicer-Lombarte, S. T. Chen, G. G. Malliaras, D. G. Barone, Foreign body reaction to implanted biomaterials and its impact in nerve neuroprosthetics. *Front. Bioeng. Biotechnol.* **9**, 622524 (2021).
23. H. Yuk, J. Wu, X. Zhao, Hydrogel interfaces for merging humans and machines. *Nat. Rev. Mater.* **7**, 935–952 (2022).
24. S. P. Lacour, G. Courtine, J. Guck, Materials and technologies for soft implantable neuroprostheses. *Nat. Rev. Mater.* **1**, 16063 (2016).
25. J. Rivnay, H. Wang, L. Fenno, K. Deisseroth, G. G. Malliaras, Next-generation probes, particles, and proteins for neural interfacing. *Sci. Adv.* **3**, e1601649 (2017).
26. N. Noskovicova, R. Schuster, S. van Putten, M. Ezzo, A. Koehler, S. Boo, N. M. Coelho, D. Griggs, P. Ruminski, C. A. McCulloch, B. Hinz, Suppression of the fibrotic encapsulation of silicone implants by inhibiting the mechanical activation of pro-fibrotic TGF-β. *Nat. Biomed. Eng.* **5**, 1437–1456 (2021).
27. Y. Liu, J. Liu, S. Chen, T. Lei, Y. Kim, S. Niu, H. Wang, X. Wang, A. M. Foudeh, J. B. Tok, Z. Bao, Soft and elastic hydrogel-based microelectronics for localized low-voltage neuromodulation. *Nat. Biomed. Eng.* **3**, 58–68 (2019).
28. K. C. Spencer, J. C. Sy, K. B. Ramadi, A. M. Graybiel, R. Langer, M. J. Cima, Characterization of mechanically matched hydrogel coatings to improve the biocompatibility of neural implants. *Sci. Rep.* **7**, 1952 (2017).
29. A. J. Vegas, O. Veiseh, J. C. Doloff, M. Ma, H. H. Tam, K. Bratlie, J. Li, A. R. Bader, E. Langan, K. Olejnik, P. Fenton, J. W. Kang, J. Hollister-Locke, M. A. Bochenek, A. Chiu, S. Siebert, K. Tang, S. Jhunjhunwala, S. Aresta-Dasilva, N. Dholakia, R. Thakrar, T. Vietti, M. Chen, J. Cohen, K. Siniakowicz, M. Qi, J. McGarrigle, A. C. Graham, S. Lyle, D. M. Harlan, D. L. Greiner, J. Oberholzer, G. C. Weir, R. Langer, D. G. Anderson, Combinatorial hydrogel library enables identification of materials that mitigate the foreign body response in primates. *Nat. Biotechnol.* **34**, 345–352 (2016).
30. M. A. Bochenek, O. Veiseh, A. J. Vegas, J. J. McGarrigle, M. Qi, E. Marchese, M. Omami, J. C. Doloff, J. Mendoza-Elias, M. Nourmohammadzadeh, A. Khan, C.-C. Yeh, Y. Xing, D. Isa, S. Ghani, J. Li, C. Landry, A. R. Bader, K. Olejnik, M. Chen, J. Hollister-Lock, Y. Wang, D. L. Greiner, G. C. Weir, B. L. Strand, A. M. A. Rokstad, I. Lacik, R. Langer, D. G. Anderson, J. Oberholzer, Alginate encapsulation as long-term immune protection of allogeneic pancreatic islet cells transplanted into the omental bursa of macaques. *Nat. Biomed. Eng.* **2**, 810–821 (2018).
31. D. Zhang, Q. Chen, Y. Bi, H. Zhang, M. Chen, J. Wan, C. Shi, W. Zhang, J. Zhang, Z. Qiao, J. Li, S. Chen, R. Liu, Bio-inspired poly-DL-serine materials resist the foreign-body response. *Nat. Commun.* **12**, 5327 (2021).
32. W. Lin, M. Kluzek, N. Iuster, E. Shimoni, N. Kampf, R. Goldberg, J. Klein, Cartilage-inspired, lipid-based boundary-lubricated hydrogels. *Science* **370**, 335–338 (2020).
33. Y. Yu, H. Yuk, G. A. Parada, Y. Wu, X. Liu, C. S. Nabzdyk, K. Youcef-Toumi, J. Zang, X. Zhao, Multifunctional "hydrogel skins" on diverse polymers with arbitrary shapes. *Adv. Mater.* **31**, e1807101 (2019).
34. S. Farah, J. C. Doloff, P. Müller, A. Sadraei, H. J. Han, K. Olafson, K. Vyas, H. H. Tam, J. Hollister-Lock, P. S. Kowalski, M. Griffin, A. Meng, M. McAvoy, A. C. Graham, J. McGarrigle, J. Oberholzer, G. C. Weir, D. L. Greiner, R. Langer, D. G. Anderson, Long-term implant fibrosis prevention in rodents and non-human primates using crystallized drug formulations. *Nat. Mater.* **18**, 892–904 (2019).
35. X. Xie, J. C. Doloff, V. Yesilyurt, A. Sadraei, J. J. McGarrigle, M. Omami, O. Veiseh, S. Farah, D. Isa, S. Ghani, I. Joshi, A. Vegas, J. Li, W. Wang, A. Bader, H. H. Tam, J. Tao, H. J. Chen, B. Yang, K. A. Williamson, J. Oberholzer, R. Langer, D. G. Anderson, Reduction of measurement noise in a continuous glucose monitor by coating the sensor with a zwitterionic polymer. *Nat. Biomed. Eng.* **2**, 894–906 (2018).
36. L. Zhang, Z. Cao, T. Bai, L. Carr, J. R. Ella-Menye, C. Irvin, B. D. Ratner, S. Jiang, Zwitterionic hydrogels implanted in mice resist the foreign-body reaction. *Nat. Biotechnol.* **31**, 553–556 (2013).
37. S. Jiang, Z. Cao, Ultralow-fouling, functionalizable, and hydrolyzable zwitterionic materials and their derivatives for biological applications. *Adv. Mater.* **22**, 920–932 (2010).
38. S. Bose, L. R. Volpatti, D. Thiono, V. Yesilyurt, C. McGladrigan, Y. Tang, A. Facklam, A. Wang, S. Jhunjhunwala, O. Veiseh, J. Hollister-Lock, C. Bhattacharya, G. C. Weir, D. L. Greiner, R. Langer, D. G. Anderson, A retrievable implant for the long-term encapsulation and survival of therapeutic xenogeneic cells. *Nat. Biomed. Eng.* **4**, 814–826 (2020).

39. F. Costa, I. F. Carvalho, R. C. Montelaro, P. Gomes, M. C. Martins, Covalent immobilization of antimicrobial peptides (AMPs) onto biomaterial surfaces. *Acta Biomater.* **7**, 1431–1440 (2011).
40. W. Whyte, D. Goswami, S. X. Wang, Y. Fan, N. A. Ward, R. E. Levey, R. Beatty, S. T. Robinson, D. Sheppard, R. O'Connor, D. S. Monahan, L. Trask, K. L. Mendez, C. E. Varela, M. A. Horvath, R. Wylie, J. O'Dwyer, D. A. Domingo-Lopez, A. S. Rothman, G. P. Duffy, E. B. Dolan, E. T. Roche, Dynamic actuation enhances transport and extends therapeutic lifespan in an implantable drug delivery platform. *Nat. Commun.* **13**, 4496 (2022).
41. E. B. Dolan, C. E. Varela, K. Mendez, W. Whyte, R. E. Levey, S. T. Robinson, E. Maye, J. O'Dwyer, R. Beatty, A. Rothman, Y. Fan, J. Hochstein, S. E. Rothenbucher, R. Wylie, J. R. Starr, M. Monaghan, P. Dockery, G. P. Duffy, E. T. Roche, An actuatable soft reservoir modulates host foreign body response. *Sci. Robot.* **4**, eaax7043 (2019).
42. D. Zhang, Q. Chen, C. Shi, M. Chen, K. Ma, J. Wan, R. Liu, Dealing with the foreign-body response to implanted biomaterials: Strategies and applications of new materials. *Adv. Funct. Mater.* **31**, 2007226 (2021).
43. J. Padmanabhan, K. Chen, D. Sivaraj, D. Henn, B. A. Kuehlmann, H. C. Kussie, E. T. Zhao, A. Kahn, C. A. Bonham, T. Dohi, T. C. Beck, A. A. Trotsyuk, Z. A. Stern-Buchbinder, P. A. Than, H. S. Hosseini, J. A. Barrera, N. J. Magbual, M. C. Leeolou, K. S. Fischer, S. S. Tigchelaar, J. Q. Lin, D. P. Perrault, M. R. Borrelli, S. H. Kwon, Z. N. Maan, J. C. Y. Dunn, R. Nazerali, M. Januszyk, L. Prantl, G. C. Gurtner, Allometrically scaling tissue forces drive pathological foreign-body responses to implants via Rac2-activated myeloid cells. *Nat. Biomed. Eng.* **7**, 1419–1436 (2023).
44. N. C. Henderson, F. Rieder, T. A. Wynn, Fibrosis: From mechanisms to medicines. *Nature* **587**, 555–566 (2020).
45. T. Zhou, H. Yuk, F. Q. Hu, J. J. Wu, F. J. Tian, H. Roh, Z. Q. Shen, G. Y. Gu, J. K. Xu, B. Y. Lu, X. H. Zhao, 3D printable high-performance conducting polymer hydrogel for all-hydrogel bioelectronic interfaces. *Nat. Mater.* **22**, 895–902 (2023).
46. J. J. Wu, H. Yuk, T. L. Sarrafian, C. F. Guo, L. G. Griffiths, C. S. Nabzdyk, X. H. Zhao, An off-the-shelf bioadhesive patch for sutureless repair of gastrointestinal defects. *Sci. Transl. Med.* **14**, eabh2857 (2022).
47. J. Wu, J. Deng, G. Theocharidis, T. L. Sarrafian, L. G. Griffiths, R. T. Bronson, A. Veves, J. Chen, H. Yuk, X. Zhao, Adhesive anti-fibrotic interfaces on diverse organs. *Nature* **630**, 360–367 (2024).
48. S. Koppaka, A. Hess-Dunning, D. J. Tyler, Biomechanical characterization of isolated epineurial and perineurial membranes of rabbit sciatic nerve. *J. Biomech.* **136**, 111058 (2022).
49. E. Ben-Menachem, Vagus nerve stimulation, side effects, and long-term safety. *J. Clin. Neurophysiol.* **18**, 415–418 (2001).
50. D. T. Plachta, M. Gierthmuehlen, O. Cota, N. Espinosa, F. Boeser, T. C. Herrera, T. Stieglitz, J. Zentner, Blood pressure control with selective vagal nerve stimulation and minimal side effects. *J. Neural Eng.* **11**, 036011 (2014).
51. H. Moon, B. Park, N. Chou, K. S. Park, S. Lee, S. Kim, Soft-actuated cuff electrodes with minimal contact for bidirectional peripheral interfaces. *Adv. Mater.* **37**, e2409942 (2024).
52. T. M. Otchy, C. Michas, B. Lee, K. Gopalan, V. Nerurkar, J. Gleick, D. Semu, L. Darkwa, B. J. Holinski, D. J. Chew, A. E. White, T. J. Gardner, Printable microscale interfaces for long-term peripheral nerve mapping and precision control. *Nat. Commun.* **11**, 4191 (2020).
53. Y. Zhang, N. Zheng, Y. Cao, F. Wang, P. Wang, Y. Ma, B. Lu, G. Hou, Z. Fang, Z. Liang, M. Yue, Y. Li, Y. Chen, J. Fu, J. Wu, T. Xie, X. Feng, Climbing-inspired twining electrodes using shape memory for peripheral nerve stimulation and recording. *Sci. Adv.* **5**, eaaw1066 (2019).
54. K. I. Song, H. Seo, D. Seong, S. Kim, K. J. Yu, Y. C. Kim, J. Kim, S. J. Kwon, H. S. Han, I. Youn, H. Lee, D. Son, Adaptive self-healing electronic epineurium for chronic bidirectional neural interfaces. *Nat. Commun.* **11**, 4195 (2020).
55. D. Rempel, L. Dahlin, G. Lundborg, Pathophysiology of nerve compression syndromes: Response of peripheral nerves to loading. *J. Bone Joint Surg. Am.* **81**, 1600–1610 (1999).
56. F. Lotti, F. Ranieri, G. Vadalà, L. Zollo, G. D. Pino, Invasive intraneural interfaces: Foreign body reaction issues. *Front. Neurosci.* **11**, 497 (2017).
57. M. Gierthmuehlen, D. T. T. Plachta, Effect of selective vagal nerve stimulation on blood pressure, heart rate and respiratory rate in rats under metoprolol medication. *Hypertens. Res.* **39**, 79–87 (2016).
58. B. W. Petkovich, J. Vega, S. Thomas, Vagal modulation of hypertension. *Curr. Hypertens. Rep.* **17**, 26 (2015).
59. T. E. Lohmeier, R. Iliescu, The baroreflex as a long-term controller of arterial pressure. *Physiology* **30**, 148–158 (2015).
60. K. Heusser, J. Tank, J. Brinkmann, J. Menne, J. Kaufeld, S. Linnenweber-Held, J. Beige, M. Wilhelmi, A. Diedrich, H. Haller, J. Jordan, Acute response to unilateral unipolar electrical carotid sinus stimulation in patients with resistant arterial hypertension. *Hypertension* **67**, 585–591 (2016).
61. J. D. Bisognano, G. Bakris, M. K. Nadim, L. Sanchez, A. A. Kroon, J. Schafer, P. W. de Leeuw, D. A. Sica, Baroreflex activation therapy lowers blood pressure in patients with resistant hypertension: Results From the double-blind, randomized, placebo-controlled rheos pivotal trial. *J. Am. Coll. Cardiol.* **58**, 765–773 (2011).
62. D. L. Bhatt, A. M. D. Kristensen, M. Pareek, M. H. Olsen, Baroreflex activation therapy for resistant hypertension and heart failure. *US Cardiol. Rev.* **13**, 83–87 (2019).
63. B. G. Fahy, Intraoperative and perioperative complications with a vagus nerve stimulation device. *J. Clin. Anesth.* **22**, 213–222 (2010).

Acknowledgments: We thank the Koch Institute Swanson Biotechnology Center for technical support, specifically K. Cormier and T. Luo at the Hope Babette Tang (1983) Histology Core for histological processing. We thank R. Bronson, a Pathologist at Harvard Medical School, and M. Boucher, a Pathologist at MIT Division of Comparative Medicine, for the histological analyses. **Funding:** This work was supported by the National Institutes of Health (1-R01HL167947-01 and 1-R01-HL153857-01) (X.Z.) and (R37NS138300) (F.W.), the Department of Defense Congressionally Directed Medical Research Programs (PR200524P1) (X.Z.), the National Science Foundation (2430106 and EFMA-1935291) (X.Z.), and a grant from the Korea Health Technology R&D Project (HI22C2190) through the Korea Health Industry Development Institute (KHIDI) funded by the Ministry of Health & Welfare, Republic of Korea (H.M.).
Author contributions: H.M., J.W., T.Z., and X.Z. conceived the idea of the ANB for nonfibrotic interfaces. H.M., J.W., and X.Z. designed the study. J.W. and H.M. developed the nonfibrotic bioelectronic interface. H.M., J.W., and J.D. synthesized the insulating layer, the conductive hydrogel, and the bioadhesive hydrogel. H.M. conducted the mechanical and electrical characterizations. H.M. and J.W. carried out the in vivo rat studies for the implantation of bioelectronic devices and histology. H.M. carried out the in vivo rat studies for BP and HR measurement upon DPN stimulation. B.F.G.A., H.M., and V.P. performed the immunofluorescence study and analysis. B.F.G.A. performed the in vitro NHS ester activity and biocompatibility experiments. H.M. prepared figures with input from all authors. H.M., B.F.G.A., J.W., F.W., and X.Z. wrote the manuscript, and all authors reviewed and edited the manuscript. J.W. and X.Z. supervised the study. **Competing interests:** X.Z. has financial interests in SanaHeal, Magnendo, and Sonologi. All other authors declare that they have no competing interests. **Data and materials availability:** All data needed to evaluate the conclusions in the paper are present in the paper and/or the Supplementary Materials.

Submitted 28 May 2025
Accepted 9 October 2025
Published 5 November 2025
10.1126/sciadv.adz3668

ScienceAdvances

Adhesive nonfibrotic bioelectronic interfaces on diverse peripheral nerves for long-term functional neuromodulation

Hyunmin Moon, Bastien F. G. Aymon, Jue Deng, Tao Zhou, Vincent Prevosto, Fan Wang, Jingjing Wu, and Xuanhe Zhao

Sci. Adv. **11** (45), eadz3668. DOI: 10.1126/sciadv.adz3668

Science Advances (ISSN 2375-2548) is published by the American Association for the Advancement of Science. 1200 New York Avenue NW, Washington, DC 20005. The title *Science Advances* is a registered trademark of AAAS.